Mesoporous Gold: Substrate-Dependent Growth Dynamics, Strain Accumulation, and Electrocatalytic Activity for Biosensing

Hyeongyu Park, Mostafa Kamal Masud,* Aditya Ashok, Minjun Kim, Md Abdul Wahab, Jun Zhou, Yukana Terasawa,* Carlos Salomon Gallo, Nam-Trung Nguyen, Md Shahriar A. Hossain, Yusuke Yamauchi, and Yusuf Valentino Kaneti*

Understanding the growth of mesoporous crystalline materials, such as mesoporous metals, on different substrates can provide valuable insights into the crystal growth dynamics and the redox reactions that influence their electrochemical sensing performance. Herein, it is demonstrated how the amorphous nature of the glass substrate can suppress the typical <111> oriented growth in mesoporous Au (mAu) films. The suppressed <111> growth is manifested as an accumulation of strain, leading to the generation of abundant surface defects, which are beneficial for enhancing the electrochemical activity. The fine structuring attained enables dramatically accelerated diffusion and enhances the electrochemical sensing performance for disease-specific biomolecules. As a proof-of-concept, the as-fabricated glass-grown mAu film demonstrates high sensitivity in electrochemical detection of SARS-CoV-2-specific RNA with a limit of detection (LoD) as low as 1 attomolar (aM).

1. Introduction

Understanding the film growth dynamics on a specific substrate is a prerequisite for preparing highly active (rough and branched) thin films with desirable optical and electrical properties.[1] In crystalline materials, the film typically grows with the same orientation and lattice parameters as the substrate, resulting in epitaxial growth. The epitaxial films can be patterned with lithography into functional devices for biomolecular detection.[2] Understanding the film growth and the nature of substrates is important for gaining better insights into the surface chemistry that influences the overall performance of an electrochemical sensing device. For

H. Park, M. K. Masud, A. Ashok, M. Kim, M. S. A. Hossain, Y. Yamauchi, Y. V. Kaneti
Australian Institute for Bioengineering and Nanotechnology (AIBN)
The University of Queensland
Brisbane, QLD 4072, Australia
E-mail: m.masud@uq.edu.au; v.kaneti@uq.edu.au

H. Park, M. S. A. Hossain
School of Mechanical and Mining Engineering
Faculty of Engineering, Architecture, and Information Technology (EAIT)
The University of Queensland
Brisbane, QLD 4072, Australia

M. A. Wahab
Energy and Process Engineering Laboratory
School of Mechanical
Medical and Process Engineering
Faculty of Science
Queensland University of Technology
2 George Street, Brisbane, QLD 4000, Australia

J. Zhou
School of Information and Communication Technology
Griffith University
Brisbane, QLD 4072, Australia

Y. Terasawa
Faculty of Advanced Science and Technology
Kumamoto University
2-39-1 Chuo-ku, Kurokami, Kumamoto-shi, Kumamoto 860–8555, Japan
E-mail: terasawa@cs.kumamoto-u.ac.jp

C. S. Gallo
Translational Extracellular Vesicles in Obstetrics and Gynae-Oncology Group and UQ Centre for Extracellular Vesicle Nanomedicine
University of Queensland Centre for Clinical Research
Faculty of Medicine
The University of Queensland
Brisbane, QLD 4029, Australia

N.-T. Nguyen
Queensland Micro- and Nanotechnology Centre (QMNC)
Griffith University
Nathan Campus, QLD 4111, Australia

Y. Yamauchi
Department of Materials Process Engineering Graduate School of Engineering
Nagoya University
Nagoya 464–8603, Japan

**ADVANCED
SCIENCE NEWS**

www.advancedsciencenews.com

**NANO · MICRO
small**

www.small-journal.com

fundamental studies of intrinsic stress, amorphous substrates are often used to remove or reduce the epitaxial mismatch effect and modify the optical and electronic properties of the deposited materials.[3] Taking surface roughness into account, the incorporation of deformable crystalline phases into a glass substrate could induce novel and intriguing properties, paving the way for promising new applications.[4]

Gold (Au) possesses a lower melting point and high atomic mobility which can lead to the formation of a thin film.[3] As a result, the bottom-up deposition approach enables the deposited Au to exhibit grain size which changes substantially with thickness, thus modifying the stress of the next deposited layer.[5] One noticeable change in the Au-glass system is the large residual stress, which can influence the functionality of electrochemical sensors. This feature is often observed in thin films during deposition.[2] For polycrystalline thin films, grain coarsening can occur during and after coalescence.[6] Therefore, it is crucial to understand the microstructural change occurring during grain coarsening in glass-grown mAu and understand its impact on the electrochemical properties. The mAu film with its small pore size, high surface-to-volume ratio, surface roughness, and inherent electrochemical properties can enable the development of low-cost and sensitive portable diagnostic devices.[7–8] Mesoporous metals possess good electrical conductivity and can greatly enhance signal transduction by delivering pore-induced large surface and interfacial bio-affinity for efficient and faster analyte binding. In particular, Au has advantages over other metals due to its good affinity toward nucleic acids (DNA, RNA), which allows for their adsorption through conventional physisorption and chemisorption mechanisms. Consequently, this can enable effective transduction and high-throughput electrochemical detection.[9–10]

Nucleic acid-driven diagnostic techniques have risen to the forefront as the preferred approach for detecting numerous chronic and infectious diseases. This prominence is due to their capacity to amplify DNA and RNA from minuscule quantities, which in turn, allows for precise and specific detection.[11] For instance, RNA-based molecular diagnostic tests with reverse transcriptase polymerase chain reaction (RT-PCR) and isothermal nucleic acid amplification technologies have been employed for COVID-19 diagnosis.[12] However, the assay requires specialized laboratories, highly trained staff, complex operation, low throughput, and expensive instrumentation.[13] The serology or rapid antibody tests provide a broad identification of past infection and immunity via an assessment of short-term (IgM, 3 to 6 days after onset) and long-term (IgG, 8 days after onset) immunoglobulin responses in patient blood. Although this assay has emerged in the past year for screening asymptomatic carriers, many questions remain to be addressed for the serological type of test as a mainstream point-of-care device due to several issues, such as antibody cross-reactivity among all six other human coronaviruses;[14] possible false-seronegative and considerably lower accuracy of the SARS-CoV-2 rapid antigen test. In

this regard, the trend in RNA detection is rapidly shifting toward advanced nanostructured biosensors, which offer advantages in molecular diagnostics, particularly in resource-limited diagnostic settings.[15] Since the discovery of the affinity of Au-based nanomaterials toward RNA, [16] many readout strategies have been developed for biomolecular detection: direct- or indirect DNA electrochemistry to labeling scheme of redox-active reporter molecules with electrochemical amplification.[17] The combination provides a distinct advantage in miniaturizing sensor design, with Au nanostructures serving as bio-receptive probes. This increases inherent sensitivity, thereby mitigating surface overload resulting from additional redox labeling or analyte amplification. As the field gradually matures, there is a paradigm shift to incorporate mesopores into the Au surface to achieve low false-negative and highly sensitive detection. In recent years, many efforts have been carried out to incorporate Au-based electrodes into affinity sensor designs for point-of-care devices. However, for the technology to be applicable in non-clinical settings, the design needs to be compatible with microfabrication processes. This enables a multiplexed configuration and ensures consistency across platforms, allowing differentiation between the surface-bound target and the unbound portion.[18]

In this study, we have selected glass substrates as they are widely used for electrochemical sensing devices due to their chemical inertness, low background signal, and ease of cleaning and calibration.[19] The fabrication of cost-effective, large-scale, and uniform mAu films on glass substrates with excellent electrochemical sensing properties remains a major engineering challenge. This study reveals the nucleation and growth dynamics of mAu on two different substrates, namely glass and silicon (Si) substrates. The findings reveal that the amorphous nature of the glass substrate can suppress the typical <111> oriented growth of Au in mAu films, leading to strain accumulation and enhanced electrochemical activity for biosensor development. Additionally, this work investigates the critical role of deposition stages in the development of robust and sensitive biosensors, facilitating the detection and quantification of nucleic acids. To demonstrate the biosensing performance of glass-grown mAu electrodes, a single-step RNA-based SARS-CoV-2 detection assay is developed with a remarkably low limit of detection (LoD) of 1 aM without the need for amplification or intricate surface modifications. It is anticipated that the engineered mAu formation on a glass substrate, detailed mechanism of growth, structural elucidation, and demonstrated proficiency in ultrasensitive RNA detection, will promote the wider utilization of mesoporous metals for biosensing applications.

2. Results and Discussion

2.1. Fabrication of mAu on Glass and Assay Principle

The fabrication of mAu on a glass substrate and the corresponding mAu-based sensor for the electrochemical sensing of SARS-CoV-2-specific RNA are illustrated in **Figure 1**. The construction of mAu on the glass substrate is carried out through standard microfabrication techniques commonly used for fabricating microdevices, sensors, and integrated circuits, followed by electrochemical deposition.[20] The method involves a few key steps that are standard in the field, including i) creation

Y. Yamauchi
Department of Chemical and Biomolecular Engineering
Yonsei University
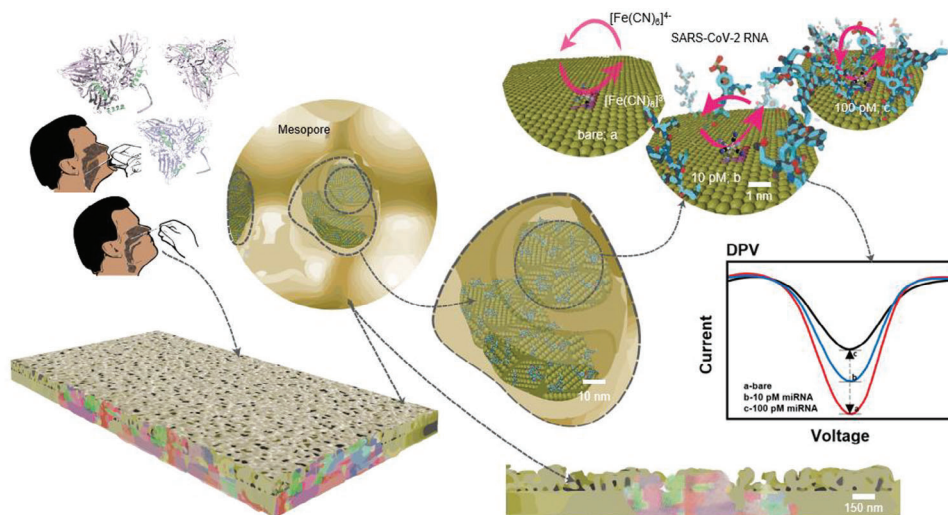Seoul 03722, South Korea

ADVANCED
SCIENCE NEWS

www.advancedsciencenews.com

NANO · MICRO
small
www.small-journal.com

Figure 1. Schematic illustration showing the development of glass-grown mAu film and its application for affinity-based electrochemical sensing of SARS-CoV-2-specific RNA without chemical and enzymatic amplification steps. A snapshot of assay construction to achieve attomolar affinity Au sensor for synthetic SARS-CoV-2; magnified images of the transducer surface during the electrochemical DPV interrogation at a level of micro- to nano-; representative readout for RNA adsorbed surface in the presence of $[Fe(CN)_6]^{3-/4-}$ redox molecules with bare, 10 pM, and 100 pM (a,b,c respectively).

of chrome-coated photomasks; ii) application of lithographic techniques for accurate patterning; iii) evaporation of Au onto the patterned glass substrate; iv) addition of a protective passivation layer; v) etching of the sputtered Au layer, and (vi) electrochemical deposition of mAu film on the glass substrate (Figure S1, Supporting Information). The dimension of the sensing area is 3 mm × 3 mm. The sensing area is separated from the non-conductive passivated layers, which are passivated with glass (silicon dioxide) and SU8, respectively. The passivation process minimizes unwanted responses during the electrochemical measurements. Approximately 200 nm of sputtered Au layer is deposited underneath the passivation layer, allowing for electron flow from the electrochemical workstation to the sensing area during electrodeposition (Figure S2, Supporting Information). Patterning for precise confinement of nanostructured surface serves as an integrated mAu transducer for the simultaneous recognition of magnetically isolated SARS-CoV-2 RNA. When a redox molecule, $Fe(CN)_6^{3-/4-}$ is present, it interacts with RNA adsorbed on mAu through well-known RNA-Au affinity interactions. These interactions follow conventional physisorption and chemisorption mechanisms, enabling the transducing process associated with the target RNA.[17] In this assay design, the target miR-SARS-CoV-2 is isolated and purified by using biotinylated capture probes and streptavidin-coated magnetic beads followed by direct adsorption of the target.[9] The underlying principle of the direct adsorption of SARS-CoV-2 RNA sequences on unmodified mAu surfaces can be explained by the well-explored nucleobases' adsorption affinity toward the bare mAu surface, where RNA bases are directly adsorbed in a sequence-dependent manner.[21] The amount of the adsorbed RNA is quantified by DPV in the presence of the $[Fe(CN)_6]^{3-}/^{4-}$ redox system. Details of the nanofabrication steps for the patterning and magnetic isolation of the lyophilized SARS-CoV-2 synthetic probe are provided in Figure S1 (Supporting Information) and the Experimental Section.

2.2. Fabrication and Optimization of Glass-Grown mAu

The typical glass-grown mAu film is prepared by electrochemically reducing Au^{3+} ions present in the micelles containing PS_{18000}-b-PEO_{7500} onto a glass surface. Herein, the polymeric micelles serve as pore-directing agents for forming uniformly sized mesopores. Figure S2 (Supporting Information) illustrates the formation of Au^{3+}-containing micelles as a sacrificial template for the fabrication of glass-grown mAu. In the electrolyte, $HAuCl_4$ is dissociated into $AuCl_4^-$ and H_3O^+ in a liquid phase and interacts with the PEO outer shell of micelles through hydrogen bonding.[7] The preferential reaction creates positively charged micelle composites that can be directed toward the surface of the working electrode.[22] The formation of micelles with $HAuCl_4$ was observed by TEM after staining with a 1% phosphotungstic acid hydrate (PTA) solution (Figure S3A,B, Supporting Information). The average size of spherical micelles obtained in the presence of Au^{3+} ions (incorporated into the hydrophilic EO moieties) (22.5 nm) is slightly larger than that of the micelles alone (20.6 nm) (Figure S3C,D, Supporting Information). A mesoporous structure is achieved after removing the residual polymer by washing or dispersing the Au films in THF at 45 °C (Figure S2, Supporting Information). Moreover, the average size of the micelles (22.5 nm) is slightly larger than the average pore diameter of the glass-grown mAu obtained with a deposition time of 100 s (Figure 2A; Figure S3D, Supporting Information).

Since the electrochemical properties of glass-grown mAu can be tuned by changing the pore size (i.e., by changing the solvent ratio), the effect of the THF:water ratio in the Au-containing electrolyte on the formation of the glass-grown mAu was investigated. The average pore size of glass-grown mAu obtained from the electrolyte containing 1 mL of THF is 13.7 nm, and the pore diameter gradually increases with increasing amount of THF (Figure S4, Supporting Information) and the corresponding DPV response also increases
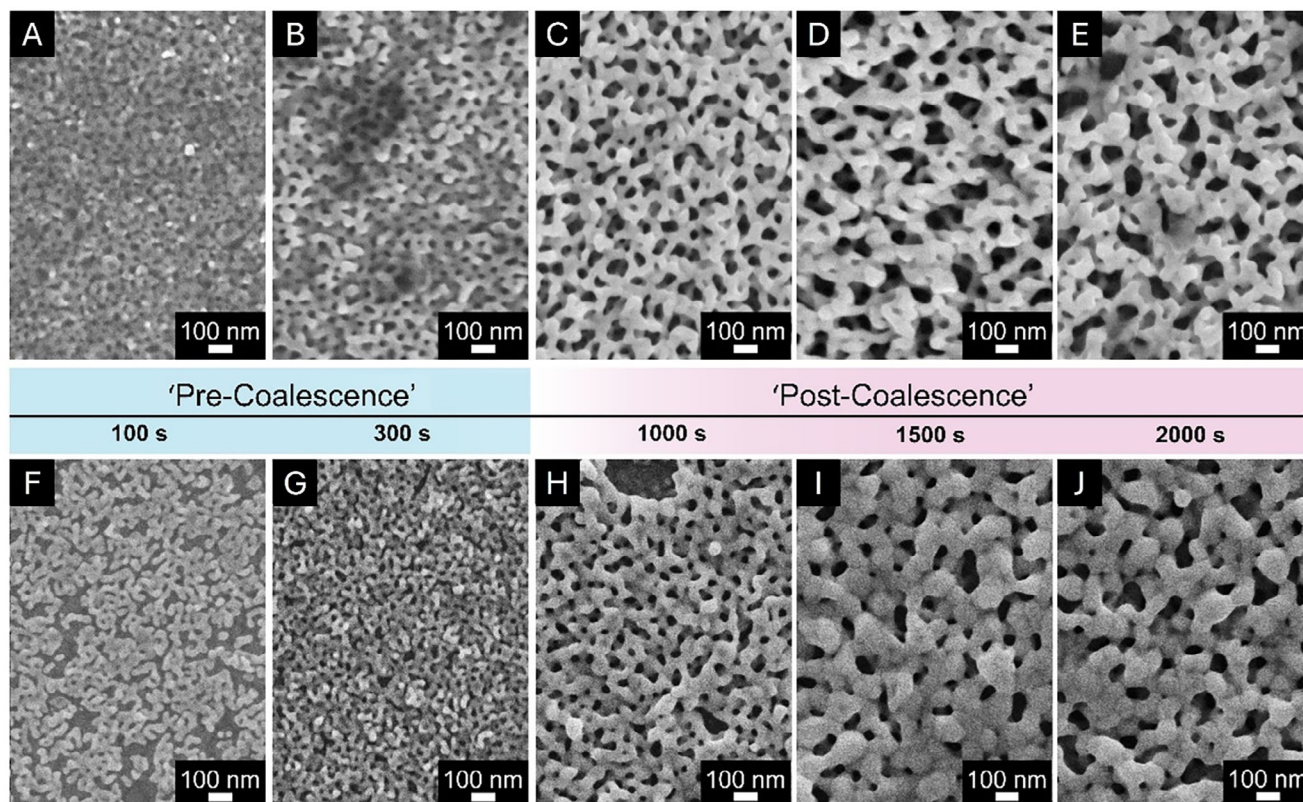
**ADVANCED
SCIENCE NEWS**

www.advancedsciencenews.com

NANO · MICRO

small

www.small-journal.com

Figure 2. A–E) Top-surface SEM images of glass-grown mAu versus F–J) Si-grown mAu films with increasing deposition time from 100 s to 2000 s were prepared with a typical electrolyte containing PS$_{18000}$-b-PEO$_{7500}$ micelles in 3 mL THF as the solvent. The glass-frown mAu films were deposited at −0.6 V versus Ag/AgCl, while the Si-grown ones were deposited at −0.5 V versus Ag/AgCl.

(Figure S5A, Supporting Information). However, the use of more than 3 mL of THF results in a decrease in both DPV response and current density (Figure S5A, Supporting Information).

For the preparation of glass-grown mAu, linear sweep voltammetry (LSV) was conducted to determine the onset reduction potential and subsequent hydrogen evolution reaction (HER) (Figure S6A, Supporting Information). The reduction of Au ions starts at ≈−0.25 V versus Ag/AgCl, and HER occurs at ≈−0.62 V versus Ag/AgCl, as indicated by the dotted lines. At ≈−0.3 V, mAu with unevenly distributed small mesopores is obtained (Figure S6B, Supporting Information). This is probably due to the reorganization of micelles in the liquid phase during the slow deposition, resulting a decrease in the DPV response and reduction current (Figure S5B, Supporting Information). As the applied potential becomes increasingly negative (−0.6 V and onwards), the surface becomes bumpy (Figure S6C,D, Supporting Information). It achieves a homogenous porous structure with relatively bigger pores. At an applied potential of −0.7 V, Au crystal growth occurs very rapidly, thus inhibiting the formation of well-dispersed pores in the resulting architecture (Figure S6D, Supporting Information). Consequently, this leads to a marked decrease in the electrochemical response (Figure S5B, Supporting Information).

A significant enhancement in the DPV response is observed at −0.5 V, suggesting a stronger interaction between the adsorbed redox molecules and the Au surface (Figure S5B, Supporting Information). Following that, we extended the deposition time from 100 to 2000 s. The SEM images of the surface clearly show that the Au films grown on glass substrates display uniformly distributed pores across the entire surface (Figure 2A–E). As the deposition time increases, the diameter of these pores expands. Concurrently, the size of ligaments or islands grows in correlation with the rate of pore expansion during the initial stage (pre-coalescence) (Figure 2A,B; Figure S7, Supporting Information), thus subsequently enhancing the DPV current response (Figure S5C, Supporting Information). After this stage, the size of the ligaments remains consistent until the Au film completes its growth (Figure 2C–E).

In contrast, the Au films grown on the Si substrate generally exhibit smaller pores than the glass-grown ones (Figure 2F–J; Figure S7, Supporting Information). Subsequently, these pores disintegrate as the deposition time is extended further (Figure 2I,J). The extended deposition period, lasting over 1000 s, induces changes in the mesoporous architecture, such as variations in pore size, expansion of ligaments or islands, and an overall impact on the material's electrochemical properties. The growth process, influenced by the characteristics of Au, such as its ductility and malleability, results in the formation of a bulk crystal structure, inhibiting well-dispersed pores and diminishing the electrochemical response. This phenomenon is particularly pronounced in mAu films grown on

**ADVANCED
SCIENCE NEWS**

www.advancedsciencenews.com

**NANO · MICRO
small**

www.small-journal.com

Si substrates, where the pores disintegrate, and the morphology becomes inflated after 1000 s of deposition (Figure 2I,J). In contrast, mAu films grown on glass maintain well-distributed mesopores, even as the film thickness increases beyond this critical deposition time (Figure 2D,E). These results reveal the superiority of the glass-grown mAu films over Si-grown ones for long-term deposition of mAu structures in practical applications.

2.3. Characterization of Glass-Grown mAu

The crystal growth of the glass-grown mAu films is significantly different from the Si-grown ones. The diffraction patterns for both films with varying deposition time were studied using grazing incident X-ray diffraction (GI-XRD) (Figures S8–S10, Supporting Information). The XRD patterns for both glass- and Si-grown mAu films show the major Au peaks, such as (111), (200), (220), and (311) (JCPDS 00-004-0784). The crystallinity of the glass-grown mAu films is better than that of Si-grown ones, which can be estimated from the significantly smaller full width at half maximum (FWHM) values (Figure S10D, Supporting Information). The GI-XRD patterns of the Si-grown mAu films show the typical (111) oriented growth. This is in good agreement with an earlier report on mAu on the Si substrate, where the deposited Au exhibited a low-index (111) plane (Figure S9, Supporting Information).[23] Notably, the relative intensities of the (200) and (220) peaks relative to (111) are much higher for glass-grown mAu films (especially for film region below 100 nm) than for Si-grown ones (Figure S10A–C, Supporting Information).

The typical growth behavior of the glass- and Si-grown mAu films is further analyzed by studying the Transmission Kikuchi diffraction (TKD) pole figures by focused ion beam (FIB) (Figure S11, Supporting Information). TKD analysis of the glass-grown mAu film suggests a more randomized orientation of the (111) plane (Figure S11A,C, Supporting Information), while the Si-grown mAu film shows a a more directed (111) orientation (Figure S11D, Supporting Infromation), as inferred from the density of TKD pole figure data points. These observations indicate that the glass-grown mAu film contains a higher fraction of high-index facets (due to the breakdown of (111) texture) that may provide more highly exposed surfaces for enhanced sensing activity relative to the Si-grown one.

The selected area electron diffraction (SAED) pattern of the cross-section of the glass-grown mAu film is shown in Figure S12 (Supporting Information). The SAED pattern viewed along the <111> direction shows the *fcc* Au (111) crystal with each of the diffraction spots widely dispersed (Figure S12 (Supporting Information), top) as opposed to the defect-free single crystal on Si (Figure S12, Supporting Information, bottom).[24] We carefully observed the steps and facets in both samples using spherical-aberration (Cs)-corrected TEM in a scanning TEM mode with a high-angle annular dark field (HAADF) (**Figure 3**). The highly magnified TEM image of the glass-grown mAu film shows a bicontinuous porous structure with a negative curvature (Figure 3A). which is reasonably in line with the top-surface SEM image in Figure 2. The HAADF-TEM analysis near the pore edge of the glass-grown mAu film shows a unique jagged structure with a higher amount of surface defects (i.e., steps) (Figure 3C).

A previous study revealed a linear relationship between the increase in surface disorder in a crystalline material and its surface reactivity.[25] Similarly, a high level of surface roughness can serve as an active sites for accelerating catalytic activity.[26] The electron beam-deposited Au (eB Au_{bottom}) on the Si and glass substrates greatly determines the preferred orientation of mAu growth. The electron beam (eB)-deposited Au on the glass substrate alone shows a small (220) initial peak, as seen in Figure S8 (Supporting Information), which facilitates the growth of premature grains with <220> direction. The higher (220)/(111) ratios in glass-grown mAu films (**Figure 4A**, left; Figure S10B, Supporting Information) suggest the preferred mAu growth along the <220> direction.[24] Furthermore, we examined the average stress exerted on the mAu films with deposition time. We compared the deformation in mAu films grown on both substrates using the classical Williamson-Hall (W-H) method.[24] The analysis derives from the total broadening peaks of GI-XRD due to the combined effect of crystallite size (β_L) and micro-strain (β_e).[24] The stress evolution derived from the W-H plot reveals that the strained regime is approximately below 100 nm for both mAu samples (mAu_{middle}), where the intensity of the peaks becomes attenuated as the thickness of mAu decreases (mAu_{top}; Figure 4A, right) in accordance with the decrease of the (220)/(111) ratio (Figure 4A, left).

The growth concerning the estimated strain of the Si-grown mAu film follows the Volmer-Web film growth in which the strain behavior resembles the glass-grown mAu but with a much steeper change in amplitude per thickness (Figure 4A, right). The mode of growth is generic and frequently observed by others and is often associated with island growth and coalescence directly. According to the model, the driving force for strain is the zipping process which reduces the overall surface energy during the grain boundary formation and accompanies the islands' elastic deformation.[6] Vigorous zipping may occur simultaneously along the ligament growth in the mAu_{middle} through sufficient elastic constraint (Figure 2A,B) followed by its stabilization with increasing deposition time (Figure 2C–E). However, for Si-grown mAu films, the ligament size is not consistent; it shows inflation beyond the 1000 s mark (Figures 2H-J). This suggests a more complex zipping activity for Si substrates, where the constraint dynamics vary, potentially due to differences in the interaction between the mAu film and the Si substrate. Noticeably, the relation of the observed stress during Volmer-Weber growth to the average grain size is found to be significantly inversed (Figure 4A, middle); glass-grown mAu_{middle} and mAu_{top} regimes seemingly generate bigger grains with an average *D* of 17.4 nm (estimated using the Scherrer's equation), as opposed to smaller grains with an average *D* of 12.1 nm for the Si-grown mAu film. The relation associated with the grain coarsening implies that growing material on an amorphous substrate may provide an efficient surface engineering strategy to remove grain boundaries and pave the way for further investigation of strain engineering for obtaining a more functional transduction surface.

In addition to these microstructural changes as tactics to drive the high catalytic activity toward oxidation, the nanostructural origin associated with the lattice under strain may also play an important role in accelerating the electrocatalytic activity. Figure 4B shows a cross-section of a typical glass-grown mAu film and the spatial-specific characterization of Kikuchi line
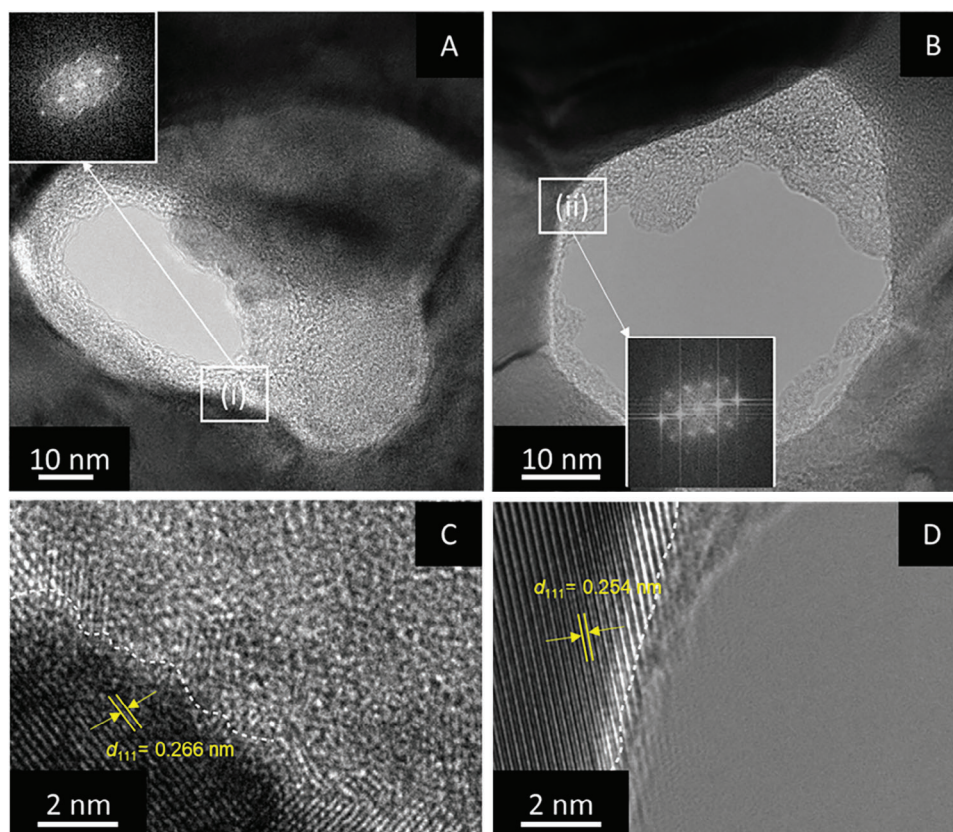
ADVANCED
SCIENCE NEWS

www.advancedsciencenews.com

NANO · MICRO
small
www.small-journal.com

Figure 3. HRTEM observations of Si- and glass-grown mAu films viewed along <111>. Determination of the quality of pore geometry from TEM images of typical A) glass-grown mAu film versus B) Si-grown mAu film and their corresponding HRTEM images for surface steps and facets (i) and (ii), respectively. The mAu film on the glass substrate was deposited at -0.6 V versus Ag/AgCl for 1500 s, whereas the mAu film on the Si substrate was deposited at -0.5 V versus Ag/AgCl for 1000 s. The THF amount was 3 mL for all films.

analysis was carried out using the electron backscatter diffraction (EBSD) mapping for both mAu films. To understand the correlation of the surface lattice structure with the catalytic activity, Kikuchi line analysis of lattice in the mAu_{middle} specific to (111) (in Figure 4C (b)) was compared with other regimes (mAu_{top} and mAu_{bottom}) but from the same (111) plane (Figure 4C (a, c)) that joined perpendicularly. From the TKD through the cross-section of a (111) beam alignment, the Kikuchi band in the mAu_{middle} (b) shows a significant shrinkage over the regimes (a, c) in their band to a greater extent over the Si-grown mAu film, suggesting the more considerable strain exerted on the glass-grown mAu film (Figure 4C). The subsets classified by the average strain and analyzed by TKD in the cross-section are, therefore, aligned with regions a, b, and c in both films, as shown in HRTEM cross-sections (Figure 4A (right) and Figure 4c,D).

As there are no previous records of a metallic structure exhibiting such a dynamic behavior under stress (which is dependent on its thickness), we assessed the electrochemical performance of both Si- and glass-grown mAu films. This investigation aimed to potentially validate the high catalytic properties of mAu. Initially, we examined the structural integrity of mAu films grown on both substrates by calculating their ECSAs (**Figure** 5A). The ECSA for each mAu film was determined by measuring the charge density associated with the reduction of Au oxide species during cyclic voltammetry (CV) in an acidic solution. For this calculation, we

assumed a charge density of 400 $\mu C\ cm^{-2}$ for deposition times of 0, 100, 300, 1000, 1500, and 2000 s. For all deposition time, glass-grown mAu is giving much higher ECSA than that of Si-grown mAu which may be due to the increased surface roughness and more exposed active sites (Figure 3C).

The thicknesses of mAu films grown on glass substrates are 46, 92, 150, 191, and 262 nm (Figures S13 and S14, Supporting Information) for deposition times of 100, 300, 1000, 1500, and 2000 s corresponding to growth rates of 0.460, 0.306, 0.150, 0.127, and 0.131 $nm\ s^{-1}$, respectively. In comparison, the thicknesses of mAu films grown on Si substrates are 31, 47, 101, 163, and 257 nm for deposition times of 100, 300, 1000, 1500, and 2000 s with the corresponding growth rates being 0.310, 0.156, 0.101, 0.108, and 0.128 $nm\ s^{-1}$, respectively (Figure 5B). Hence, the glass-grown mAu films are generally thicker than the Si-grown ones.

To gain insights into the impact of strain engineering on the electrochemical performance, we observed the current reduction per ECSA for mAu films grown on both Si and glass substrates. The differential pulse voltammetry (DPV) responses are similar on both substrates for bare films (at 0 s) and films deposited for 100 s (Figure S13, Supporting Information), indicating that the reduction of $[Fe(CN)_6]^{3-/4-}$ is not influenced by passivating materials, such as SiO_2 and SU8 across these films (Figure S1, Supporting Information). However, above 100s, the glass-grown
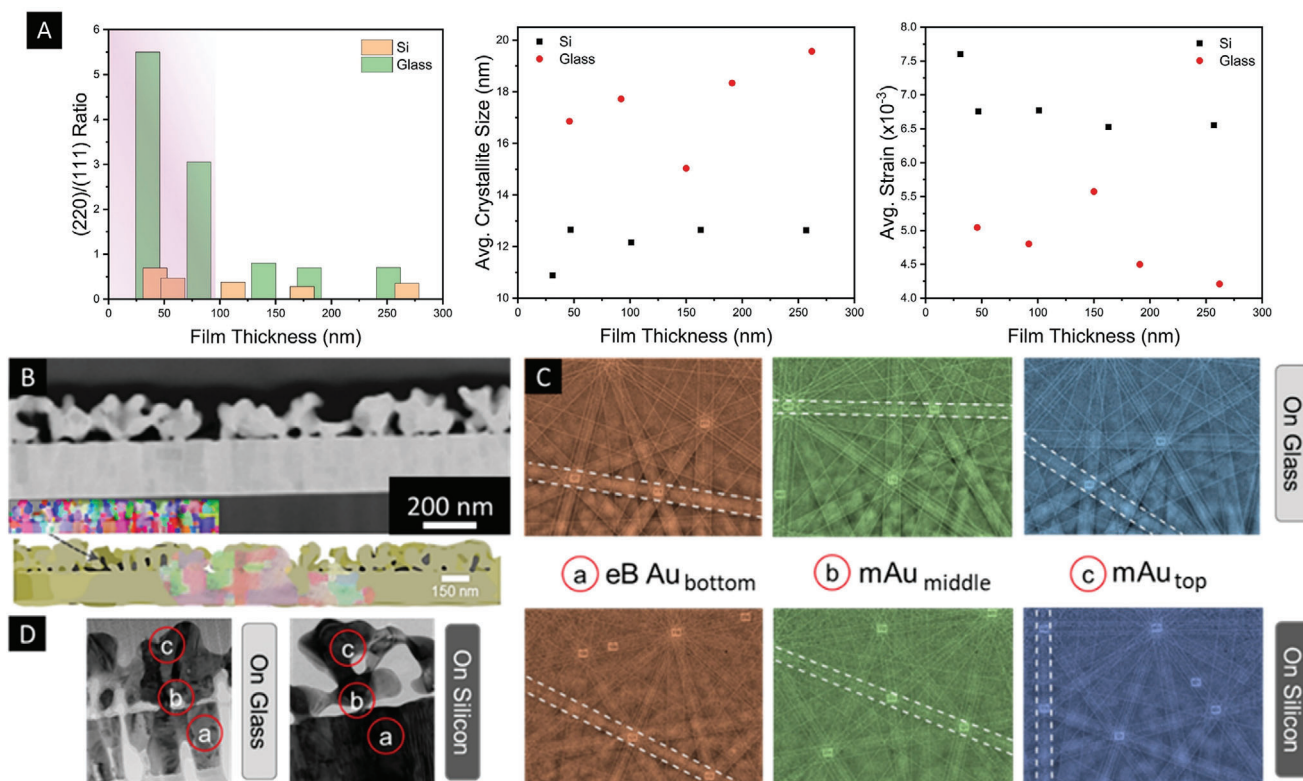
ADVANCED
SCIENCE NEWS

www.advancedsciencenews.com

NANO · MICRO
small

www.small-journal.com

Figure 4. The stress evolution model for glass-grown and Si-grown mAu films. A) The relative intensity ratio of Au(220) to Au(111) (*left*); The average crystallite size (*D*) was calculated using Scherrer's equation derived from the GI-XRD (*middle*) and the strain developed in the given samples derived from peak broadening (*βe*) using the Williamson-Hall (W-H) method (*right*).[24] B) TKD orientation mapping of glass-grown mAu C) Kikuchi lines formed by TKD measurements of crystal phase for a, b, c. D) Subsets classified by the estimated average strain; representative thickness specific to electron beam (eB)-deposited Au (eB Au$_{bottom}$) (a), mAu$_{middle}$ (b; below 100 nm), and mAu$_{top}$ (c; above 100 nm). The mAu films grown on the glass substrates in Figure 4A were deposited at −0.6 V versus Ag/AgCl, whereas the mAu films grown on the Si substrates in Figure 4A were deposited at −0.5 V versus Ag/AgCl. The THF amount was 3 mL for all films. The glass-grown and Si-grown mAu films used for the TKD measurements in Figure 4B-D were obtained using an applied potential of −0.6 V versus Ag/AgCl for 1500 s and −0.5 V versus Ag/AgCl for 1000 s, respectively.

mAu films show higher current responses when normalized by the physical surface area (length × width) with respect to the deposition time (Figure 5C). Furthermore, the current generated by the glass-grown mAu films is notably higher than that of Si-grown mAu films per ECSA (Figure 5D). This enhancement is attributed to the micro-to-nano structural response to deformation within the mAu$_{middle}$ film on the glass substrate, arising from the strained regime located ∼below 100 nm (Figure 4C). The enhanced ligament growth in the glass-grown mAu film is facilitated by the merging of islands during elastic formation, leading to significant structural relaxation. Furthermore, the rich surface defects in the glass-grown mAu film (Figure 3C3C) can provide abundant active sites for accelerating its electrocatalytic activity.

2.4. RNA Surface Interaction on Glass-Grown Mesoporous Au Assembly

Detection of genetic components (RNA, DNA) is becoming increasingly important with the emergence of new infectious diseases, such as SARS-CoV-2. The conventional detection methods use amplification techniques (e.g., PCR, rolling circle am-

plification, and enzymatic amplification) and require sophisticated laboratories, trained personnel, and bioreagents, making these techniques expensive and unsuitable in resource-limited settings.[26] The DNA-Au affinity interactions chemistry combined with an electrochemical transducer has evolved as one of the most cost-effective and robust technologies for genetic material sensing. The integration of mAu architecture with an electroconductive framework further enhances signal transduction and facilitates the direct adsorption of nucleic acids (DNA, RNA).[9] The direct adsorption of nucleic acids follows conventional physisorption and chemisorption mechanisms. This entails the direct interaction of nitrogen atoms from the nucleobase ring with Au in its zero state, along with a partial contribution from the exocyclic amino group and charge transfer between the aromatic ring and the gold surface.[27] To check the oxidation state of our as-prepared mAu on glass, we employed X-ray photoelectron spectroscopy (XPS) (Figure S15, Supporting Information). This analysis confirms the zero-valent state (Au^0) of Au is maintained. Moreover, the zero-valent Au is preferable for biosensing over the (Au$^+$) and (Au^{3+}) state of Au due to its resistance to oxidation in air and higher stability in strong alkalis and acids. It can also be noted that an increase in the binding energy for the O1s peak (at ≈532 eV) in our XPS data suggests

**ADVANCED
SCIENCE NEWS**
www.advancedsciencenews.com
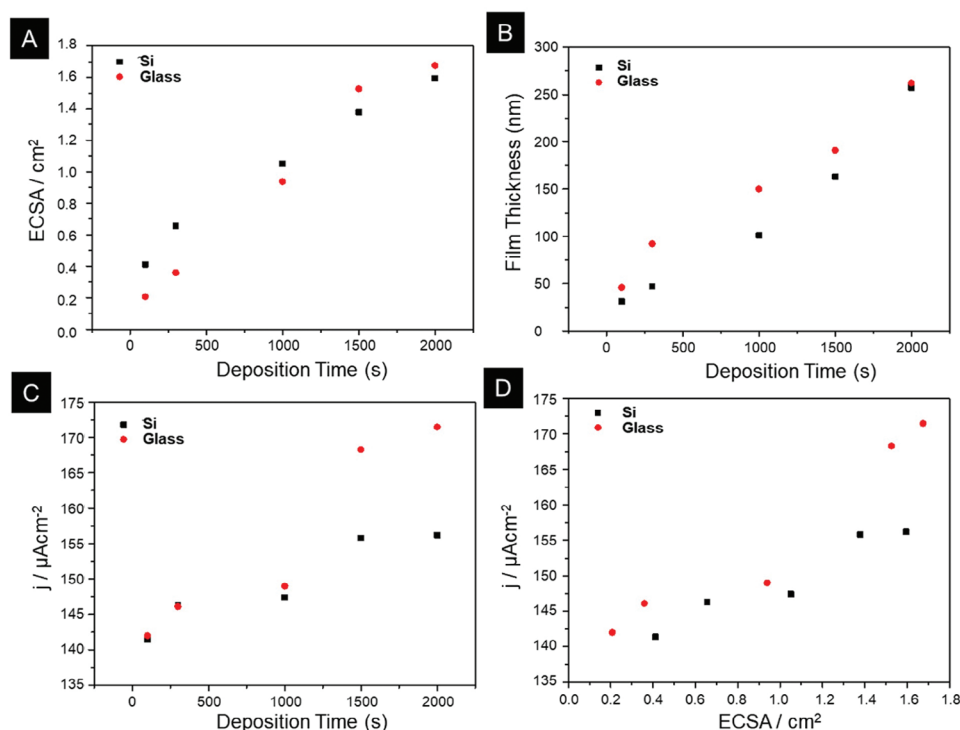
NANO · MICRO
small
www.small-journal.com

Figure 5. A) Electrochemically active surface areas (ECSAs) of mAu films grown on Si and glass substrates with varying deposition times from 100 s to 2000 s. B) Variations in film thickness of Si- and glass-grown mAu films with increasing deposition time. C) DPV responses of Si- and glass-grown mAu films in a solution of 2.5 mM $[Fe(CN)_6]^{3-/4-}$ (0.1 M KCl, 10 mM PBS; pH 7.4), normalized by the physical surface area (length × width) with respect to the deposition time. D) Current responses with respect to ECSA for both glass- and Si-grown mAu films. The glass-grown mAu films were obtained at −0.6 V versus Ag/AgCl, whereas the Si-grown ones were obtained at −0.5 V versus Ag/AgCl. The THF amount was 3 mL for all films.

a higher presence of hydroxyl groups or water on the surface of glass-grown mAu film, potentially enhancing the biosensing performance by improving surface hydrophilicity and enabling more effective interactions with the target molecules. Based on the above findings, we have designed a proof-of-concept assay for detecting SARS-CoV-2 specific-RNA using the typical glass-grown mAu film deposited for 1500 s at −0.6 V versus Ag/AgCl. This glass-grown mAu film was selected due to the higher current generated per ECSA (Figure 5D) and saturation of the DPV response at 1500 s (Figure S5C, Supporting Information). In this assay design, the virus' genetic material RNA is extracted and purified from a spiked sample (Figure 1 and **Figure 6A**). First, we confirm the efficacy of target RNA sequence isolation by challenging the glass-grown mAu surface with target sequences using positive RNA that contains both targets, lineage B-βCoV and SARS-CoV-2 (2019-nCoV RUO Kit). The results show that the charges generated for the target RNA sequence (i.e., SARS-CoV-2) by DPV interrogations are much higher and distinguishable from the bare sensor (Figure 6B,C). These identical experiments provide good reproducibility, indicating the universality of our isolation technique (details of magnetic isolation and purification steps are provided in the Experimental Section). Next, we determine the maximum interaction of magnetically isolated SARS-CoV-2 RNA with redox molecules. This is achieved by conducting electrical measurements on surface-bound RNA attached to glass-grown mAu films with different thicknesses using the same RNA concentration. With standard 10 pM target RNA sequences,

the DPV response of the glass-grown mAu film follows a typical dose-response curve in which the RNA-Au affinity saturates at a deposition time of 1500 s (thickness of around 190 nm), and the increment of the total charge for subsequent deposition time is no longer significant (Figure 6D). This is possible because the fraction of the electric repulsion between negatively charged RNA and negatively charged $[Fe(CN)_6]^{3-/4-}$ redox system decreases relative to the total ECSA as the film thickness increases.

2.5. Validation of Redox Mediated Electrocatalytic Activity and Sensing

The glass-grown mAu film generates significantly enhanced cathodic (j_{pc}) and anodic (j_{pa}) peak currents (Figure S16A,B, Supporting Information). It is also capable of boosting both the redox process of the $[Fe(CN)_6]^{3-/4-}$ system, owing to a more exposed Au surface with highly engineered structural and crystallographic properties (Figure S10, Supporting Information). To assess the potential of the glass-grown mAu as a detection platform for SARS-CoV-2, we performed the CV measurements at different scan rates (ν) (Figure S17A, Supporting Information). The curve reveals that both j_{pc} and j_{pa} increase proportionally with the increase of scan rate from 0.01 to 1 V s^{-1}. In addition, they show linear relationships with $\nu^{1/2}$, suggesting that the reaction kinetics of the electrode are mainly diffusion-controlled, thus confirming
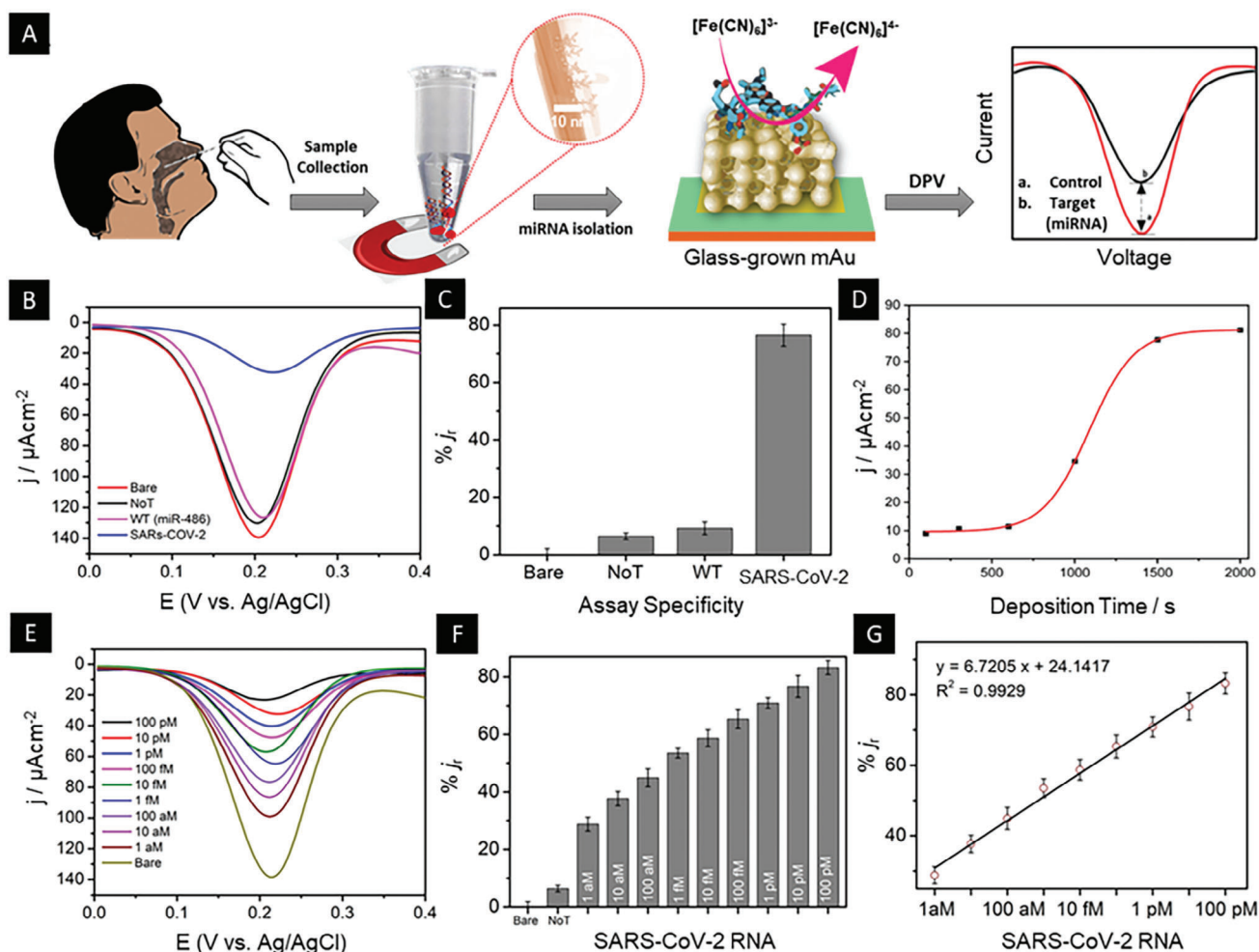
**ADVANCED
SCIENCE NEWS**

www.advancedsciencenews.com

NANO · MICRO

small

www.small-journal.com

Figure 6. Electrochemical analysis of transducer surface-bound RNA in 2.5 mM $[Fe(CN)_6]^{3-/4-}$ solution (0.1 M KCl, 10 mM PBS; pH 7.4). A) Schematic representation of the assay design using the positive sequence from RealStare® SARS-CoV-2 RT-PCR kit (Altona). B,C) DPV responses of no-template control (NoT) and wrong-target (non-complementary sequence; miR-338–3p) and the corresponding bar diagram; D) electrodeposition time versus DPV responses of surface-bound 10 pM RNA with increasing film thickness; E) DPV responses of synthetic target SARS-CoV-2 RNA with different concentrations, ranging from 100 pM to 1 aM; F) the corresponding bar diagram and G) linear correlation for LoD estimation. Here, the glass-grown mAu film used for the electrochemical tests was obtained at an applied potential of −0.6 V versus Ag/AgCl with a deposition time of 1500 s and a THF amount of 3 mL.

that the studied scan rates are suitable for further electrocatalytic studies. The corresponding current responses also show a steep slope with a value of 5.16 (for j_{pc}), thereby verifying the superior catalytic activity of glass-grown mAu toward the redox reaction of $[Fe(CN)_6]^{3-/4-}$ (Figure S17B, Supporting Information). Next, we recorded the chronoamperometric (CA) responses of this glass-grown mAu film to observe if the high j_{pc} results from the increased surface affinity to redox substrates. Upon successive additions of $[Fe(CN)_6]^{3-/4-}$ solution, the CA response increases steeply (Figure S17C, Supporting Information). The calibration curve follows the characteristic Michaelis-Menten equation.[27] The apparent Michaelis-Menten constant ($K_{m\ app}$) can be obtained from the electrochemical version of the Lineweaver-Burk model, which is estimated to be 0.3527 (Figure S17D, Supporting Information), which is very low, indicating the high-affinity mAu toward the redox system.[27] Besides, the glass-grown mAu film

possesses high stability as it can maintain signal generation over multiple CV cycles of 40 in both basic (2.5 mM $Fe(CN)_6^{3-/4-}$) and acidic (0.5 M H_2SO_4) media (Figure S18A,B, Supporting Information). It can also retain its integrity and functionality even after undergoing cleaning protocols, like acid washing, and therefore, can be reused. This aligns with research on the universal approach to synthesizing mAu films, which indicates that such films are well-suited for electrocatalysis and, by extension, electrochemical sensing.[28] The fabrication method highlighted in this study ensures the durability and functional properties of the mAu films are preserved post-cleaning, reinforcing the potential for their repeated use in sensing applications. The stability of the glass-grown mAu film in acidic media along with its reproducibility and strong affinity toward redox molecules render it highly attractive for signal transduction in electrochemical biosensing.

**ADVANCED
SCIENCE NEWS**

www.advancedsciencenews.com

**NANO · MICRO
small**

www.small-journal.com

2.6. Specificity and Sensitivity of the Glass-Grown mAu Sensor

The SARS-CoV-2 RNA detection assay is depicted in Figure 6A. Briefly, magnetically isolated SARS-CoV-2 RNA was adsorbed onto the mAu surface followed by DPV interrogation in the presence of a redox marker, $Fe(CN)_6^{3-/4-}$. The SARS-CoV-2 RNA sequence was isolated and purified using a target-complementary biotinylated capture probe and a magnetic streptavidin-labeled Dynabead following our previously published papers.[8a,17,24] This step provides the purified target sequence to avoid interference from other non-specific biomolecules or sequences, especially from negatively charged species. We tested the specificity of our assay by challenging the wrong target (a different sequence than the target RNA) along with a system control study. It can be observed from Figure 6B,C that both the NoT (PBS was used instead of RNA sample) and wrong target (miR-338) generate negligible current responses (relative activities are 6.42% and 9.28%, respectively), while the same concentration of (10 pM) of target generates an activity of 76.23%. This experiment, which highlights the negligible background noise originating from the potential influence of other species with negative charges in the glass-grown mAu transduction system, reinforces the high specificity of our assay. The strategic inclusion of diverse controls, such as the no-template control and non-complementary sequence experiments, allows for a rigorous assessment of specificity by systematically examining the differences in current responses. Moreover, along with high specificity, the assay needs to be highly sensitive, so that it can quantify the very small changes in RNA expression in relation to the disease. To assess the sensitivity of our assay, we have extracted the target RNA from the different concentrations of spiked samples ranging from 1 aM to 100 pM. Following the magnetic bead-based isolation and purification, the extracted RNAs are adsorbed onto the glass-grown mAu transduction surface. It can be seen from Figure 6E,F that with the increase of RNA concentration in the spiked sample, the relative activity (current response) increases. This can be explained by the fact that more RNA can cover a higher amount of transduction surface, thereby blocking the surface that ultimately reduces the current in response to the bare transduction surface. The activity for different concentrations follows a linear trend over the studied concentrations (Figure 6G). The lowest concentration 1 aM, shows more than four times higher activity than that of the control (NoT; 22.80% versus 6.42%) and three times higher response than that of the wrong target (22.80% versus 9.28%). We estimate the assay sensitivity by considering s/n = 3, which is 1 aM. Our assay performance is highly comparable to or even superior to recently reported nanomaterials-based RNA sensors (Table S1, Supporting Information).[29–36] For instance, our RNA assay is more sensitive (1 aM versus 2.2 fM) than the recently reported assay using 3D popcorn-like Au nanofilms.[30] Moreover, this assay required target recycling steps, whereas our assay is direct and does not require any enzymatic or chemical amplification steps. There is a report that achieved a 3 aM level of sensitivity, however, this assay involved a multi-step junction formation as well as enzymatic cleavage steps.[36] The high sensitivity of our assay is due to the optimized formation of lattice-matched mAu on the glass surface. This high sensitivity is expected to be highly beneficial for tracing small genetic changes. This assay is robust, rapid (it takes 30 min to analyze a purified RNA sample), and highly sen-

sitive, which is not only useful for SARS-CoV-2 but may also be useful for detecting RNA biomarkers in other infectious diseases.

3. Conclusion

This work presents a facile soft-templating electrodeposition method for fabricating mAu films on glass substrates without epitaxial stress. The proposed approach offers a straightforward means of depositing mAu films on glass surfaces, while also identifying high-index surfaces for achieving highly active transduction. The glass-grown mAu film undergoes stress evolution unique to its sub-thickness, inducing strain by reducing surface energy. The region of glass-grown mAu with maximum strain exhibits accelerated diffusion rates compared to Si-grown mAu. Additionally, the glass-grown mAu film, featuring distinctive pore geometry and large pores, holds promise for developing proof-of-concept assays for specific RNA detection and quantification of SARS-CoV-2 with a sensitivity of 1 aM. This advancement can facilitate the diagnosis of infectious diseases in resource-limited settings, offering a cost-effective solution.

4. Experimental Section

Reagents and Materials: Gold(III) chloride, tetrahydrofuran (THF), potassium hexacyanoferrate (II), potassium hexacyanoferrate (III), and phosphate buffer saline (PBS) tablet (0.01 M phosphate buffer, 0.0027 M potassium chloride and 0.137 M sodium chloride, pH 7.4 at 25 °C) were purchased from Sigma-Aldrich (Australia). Polystyrene-*block*-poly(ethylene oxide) (PS-*b*-PEO) diblock copolymer was obtained from Polymer Source Inc. (Canada). Tris was purchased from VWR Life Science (Australia). All chemicals and reagents were used as received without additional purification. Oligonucleotides were acquired from Integrated Technologies, USA. The probe sequences for the ORF1b gene assay were 5′-TAGTTGTGATGCWATCATGACTAG-30 (Probe in 5′-FAM/ZEN/3′-IBFQ format; w = A/T) with biotinylated capture probe (CTA GTC ATG ATT GCA TCA CAA CTA/3Biotin/) and Synthetic SARS-CoV-2 sequence (UCU UUG GUU AUC UAG CUG UAU GA).

Microfabrication: L-edit software was used to draw the design on a 6″ pure silicate (100) wafer. The wafers were cleaned with acetone, isopropanol, and deionized water under sonication. Next, the wafers were spin-coated and soft-baked with the negative photoresist AZ2020. Next, the wafers were patterned via UV exposure, followed by hard baking. The lithography was completed by a direct laser writing system (Heidelberg uPG101 laser writer). Next, 20 nm titanium and 200 nm Au layers were deposited by electron beam evaporation (Temescal FC-2000 e-beam evaporator) at a pressure of 10^{-6} Torr after the surface treatment by oxygen plasma for 5 min on Oxford RIE. The lift-off of the patterned Au was performed using remover PG. Insulating silicon dioxide or SU8 was deposited for the passivation layer using a sputter coating system, while the commercial developer and metal etchant were used for developing, etching, and exposure.

Fabrication of Mesoporous Au (mAu) Films: The mAu films were fabricated by a soft-templating approach using PS_{18000}-*b*-PEO_{7500} (Poly(styrene)-*block*-poly(ethylene glycol)) block copolymer. This block copolymer served as a pore-directing agent for obtaining mesopores in the Au film on a patterned glass substrate. In a typical procedure, 10 mg of the PS-*b*-PEO block copolymer was dissolved in 3 mL of THF and then stirred for 8 h to enable the block copolymer to form the PS-core of the template. Following this, 1 mL of $HAuCl_4$ as Au precursor was added dropwise with the successive addition of 2.5 mL of deionized water. The Au precursor was incorporated into the PEO shell, while the added water facilitated the self-assembly of the block copolymer micelles in the solution. Then, the mAu film was deposited on the patterned glass substrate via an

electrochemical deposition at −0.5 V versus Ag/AgCl for 1000 s, using a CHI660 electrochemical workstation (CH Instruments, USA). The mAu film was then immersed in THF at 45 °C for 15 s three times at an interval of 2 s to remove the residual block copolymer.

Characterization: The morphology of the mAu films was checked by scanning electron microscope (SEM, Hitachi 7100, Japan). The crystal structures of the mAu films were analyzed by Grazing Incidence X-ray Diffraction (GI-XRD) using a Rigaku SmartLab system set to an in-plane configuration. The system employed a Cu Kα radiation source with a current of 200 mA, a voltage of 45 kV, and a scan rate of 0.5° min⁻¹. The lattice imaging and selected area electron diffraction (SAED) patterns of the mAu samples were acquired using a transmission electron microscope (Hitachi HF5000), equipped with a Oneview CMOS camera from Gatan, Inc., USA, operated at an acceleration voltage of 200 kV. The surface elemental analysis was carried out using X-ray Photoelectron Spectroscopy (XPS) (Kratos Axis Supra+ with monochromatic Al Kα X-rays (1486.6 eV)). A focused ion beam (FIB) system was utilized to precisely mill a lamellar section from the mAu film for transmission Kikuchi diffraction (TKD) analysis. The electron backscatter diffraction (EBSD) detector was optimized for TKD mode.to enhance the depth of structural characterization. Analysis of Kikuchi patterns was done using Aztec Crystal software.

Magnetic Isolation of Lyophilized SARS-CoV-2 Synthetic Probe: The target miRNA was isolated and purified from the spiked sample following previously published protocols.[21,37] Briefly, the spiked RNA (total RNA) sample was adjusted to the required concentration in 5 μL of RNase-free water before mixing with 10 μL of 5X saline-sodium citrate (SSC) buffer and 10 μL of 10 μM biotinylated capture probes. After heating the mixture at 60 °C for 2 min followed by incubation for 60 min at room temperature. For magnetic isolation of target sequence, 5 μL of streptavidin-labeled Dynabeads MyOne Streptavidin C1 (Invitrogen) magnetic beads were washed and resuspended in 10 μL of 2X B&W buffer. Then, the resuspended magnetic beads were added to the prepared capture probes-target RNA hybrid. After 30 min incubation, the magnetic bead-hybrid structure was washed and heated at 95 °C to release the target RNA. An external magnet collected the magnetic bead-capture probe, and the released target RNA was collected within a short time. Before applying RNA to the glass-grown mAu film, the RNA was diluted two times with 5X SSC buffer.

Electrochemical Measurement of Catalytic Activity: A total of 5.0 μL (diluted in 5X SSC buffer) of the synthetic SARS-CoV-2 sequence was adsorbed on the surface of the glass-grown mAu film. After 30 min of incubation, the electrode was washed (gently) with phosphate-buffered saline (PBS) (three times). The differential pulse voltammetry (DPV) experiments were recorded at −0.1 to −0.5 V with a pulse amplitude of 50 mV and a pulse width of 50 ms in 10 mM PBS solution containing 2 mM [$K_3Fe(CN)_6$] and 2 mM [$K_4Fe(CN)_6$] electrolyte solution (0.1 M KCl, 10 mM PBS; pH 7.4) before and after adsorbing target RNA on the surface of the glass-grown mAu film. The relative DPV current changes (i.e., %$i_{Relative}$, percent difference of the DPV signals generated for captured RNA (i_{RNA}) concerning the baseline current ($i_{Baseline}$) due to the adsorption of RNA were then measured by using the following equation:

$$\%j_{Relative} = \left(\left(j_{Baseline} - j_{RNA} \right) / j_{Baseline} \right) \times 100 \tag{1}$$

where $j_{Baseline}$ and j_{RNA} are current densities obtained for bare electrode and electrode after RNA adsorption, respectively.

Supporting Information

Supporting Information is available from the Wiley Online Library or from the author.

Conflict of Interest

The authors declare no conflict of interest.

Data Availability Statement

The data that support the findings of this study are available in the supplementary material of this article.

[1] P. Malinský, P. Slepička, V. Hnatowicz, V. Švorčík, *Nanoscale Res. Lett.* **2012**, *7*, 241.

[2] E. Chason, P. R. Guduru, *J. Appl. Phys.* **2016**, *119*, 191101.

[3] T.-A. Truong, T.-K. Nguyen, H. Zhao, N.-K. Nguyen, T. Dinh, Y. Park, T. Nguyen, Y. Yamauchi, N.-T. Nguyen, H.-P. Phan, *Small* **2022**, *18*, 2105748.

[4] T. Egami, *Prog. Mater. Sci.* **2011**, *56*, 637.

[5] Z. Kolska, J. Riha, V. Hnatowicz, V. Svorcik, *Mater. Lett.* **2010**, *64*, 1160.

[6] J. A. Floro, S. J. Hearne, J. A. Hunter, P. Kotula, E. Chason, S. C. Seel, C. V. Thompson, *J. Appl. Phys.* **2001**, *89*, 4886.

[7] C. Li, B. Jiang, H. Chen, M. Imura, L. Sang, V. Malgras, Y. Bando, T. Ahamad, S. M. Alshehri, S. Tominaka, Y. Yamauchi, *Nano Res.* **2016**, *9*, 1752.

[8] A. Ashok, T. K. Nguyen, M. Barton, M. Leitch, M. K. Masud, H. Park, T. A. Truong, Y. V. Kaneti, H. T. Ta, X. Li, *Small* **2022**, 2204946.

[9] M. K. Masud, J. Na, T.-E. Lin, V. Malgras, A. Preet, A. A. Ibn Sina, K. Wood, M. Billah, J. Kim, J. You, K. Kani, A. E. Whitten, C. Salomon, N.-T. Nguyen, M. J. A. Shiddiky, M. Trau, M. S. A. Hossain, Y. Yamauchi, *Biosens. Bioelectron.* **2020**, *168*, 112429.

[10] Y. Kang, M. K. Masud, Y. Guo, Y. Zhao, Z. S. Nishat, J. Zhao, B. Jiang, Y. Sugahara, T. Pejovic, T. Morgan, *ACS Nano* **2023**, *17*, 3346.

[11] M. M. Kaminski, O. O. Abudayyeh, J. S. Gootenberg, F. Zhang, J. J. Collins, *Nat. Biomed. Eng.* **2021**, *5*, 643.

[12] L. J. Carter, L. V. Garner, J. W. Smoot, Y. Li, Q. Zhou, C. J. Saveson, J. M. Sasso, A. C. Gregg, D. J. Soares, T. R. Beskid, S. R. Jervey, C. Liu, *ACS Cent. Sci.* **2020**, *6*, 591.

ADVANCED
SCIENCE NEWS

www.advancedsciencenews.com

NANO · MICRO
small

www.small-journal.com

[13] B. Udugama, P. Kadhiresan, H. N. Kozlowski, A. Malekjahani, M. Osborne, V. Y. C. Li, H. Chen, S. Mubareka, J. B. Gubbay, W. C. W. Chan, *ACS Nano* **2020**, *14*, 3822.

[14] W. N. Chia, C. W. Tan, R. Foo, A. E. Z. Kang, Y. Peng, V. Sivalingam, C. Tiu, X. M. Ong, F. Zhu, B. E. Young, M. I. C. Chen, Y.-J. Tan, D. C. Lye, D. E. Anderson, L.-F. Wang, *Emerg Microbes Infect* **2020**, *9*, 1497.

[15] R. Mirzaei, F. Mahdavi, F. Badrzadeh, S. R. Hosseini-Fard, M. Heidary, A. S. Jeda, T. Mohammadi, M. Roshani, R. Yousefimashouf, H. Keyvani, M. Darvishmotevalli, M. Z. Sani, S. Karampoor, *Int. Immunopharmacol.* **2021**, *90*, 107204.

[16] K. Saha, S. S. Agasti, C. Kim, X. Li, V. M. Rotello, *Chem. Rev.* **2012**, *112*, 2739.

[17] T. G. Drummond, M. G. Hill, J. K. Barton, *Nat. Biotechnol.* **2003**, *21*, 1192.

[18] M. K. Masud, M. Umer, M. S. A. Hossain, Y. Yamauchi, N.-T. Nguyen, M. J. A. Shiddiky, *Trends Biochem. Sci.* **2019**, *44*, 433.

[19] V. Lacmanova, J. Leitner, P. Hausild, J. Cech, J. Nohava, P. Sajdl, A. Michalcova, A. Slepicka, A. Reznickova, *Vacuum* **2023**, *212*, 111991.

[20] F. J. Tovar-Lopez, *Sensors* **2023**, *23*, 5406.

[21] M. N. Islam, M. K. Masud, N.-T. Nguyen, V. Gopalan, H. R. Alamri, Z. A. Alothman, M. S. A. Hossain, Y. Yamauchi, A. K. Lamd, M. J. A. Shiddiky, *Biosens. Bioelectron.* **2018**, *101*, 275.

[22] C. Li, Ö. Dag, T. D. Dao, T. Nagao, Y. Sakamoto, T. Kimura, O. Terasaki, Y. Yamauchi, *Nat. Commun.* **2015**, *6*, 6608.

[23] K. Zhang, X. B. Pitner, R. Yang, W. D. Nix, J. D. Plummer, J. A. Fan, *Proc Natl Acad Sci U S A* **2018**, *115*, 685.

[24] P. Mondal, D. Das, *RSC Adv.* **2015**, *5*, 54011.

[25] C. Xie, D. Yan, W. Chen, Y. Zou, R. Chen, S. Zang, Y. Wang, X. Yao, S. Wang, *Mater. Today* **2019**, *31*, 47.

[26] P. Craw, W. Balachandran, *Lab Chip* **2012**, *12*, 2469.

[27] M. K. Masud, M. N. Islam, M. H. Haque, S. Tanaka, V. Gopalan, G. Alici, N.-T. Nguyen, A. K. Lam, M. S. A. Hossain, Y. Yamauchi, *Chem. Commun.* **2017**, *53*, 8231.

[28] H. Lim, K. Kani, J. Henzie, T. Nagaura, A. S. Nugraha, M. Iqbal, Y. S. Ok, M. S. A. Hossain, Y. Bando, K. C. W. Wu, H.-J. Kim, A. E. Rowan, J. Na, Y. Yamauchi, *Nat. Protoc.* **2020**, *15*, 2980.

[29] Y. Zhao, C. Lu, X.-E. Zhao, W. Kong, S. Zhu, F. Qu, *Biosens. Bioelectron.* **2022**, *208*, 114215.

[30] H. Zhou, J. Zhang, B. Li, J. Liu, J.-J. Xu, H.-Y. Chen, *Anal. Chem.* **2021**, *93*, 6120.

[31] J. Dong, L. Wen, H. Yang, J. Zhao, C. He, Z. Hu, L. Peng, C. Hou, D. Huo, *Anal. Chem.* **2022**, *94*, 5846.

[32] J. Bao, C. Hou, Y. Zhao, X. Geng, M. Samalo, H. Yang, M. Bian, D. Huo, *Talanta* **2019**, *196*, 329.

[33] C. Pothipor, J. Jakmunee, S. Bamrungsap, K. Ounnunkad, *Analyst* **2021**, *146*, 4000.

[34] C. Pothipor, N. Aroonyadet, S. Bamrungsap, J. Jakmunee, K. Ounnunkad, *Analyst* **2021**, *146*, 2679.

[35] L. Zhou, Y. Wang, C. Yang, H. Xu, J. Luo, W. Zhang, X. Tang, S. Yang, W. Fu, K. Chang, *Biosens. Bioelectron.* **2019**, *126*, 657.

[36] L. Yu, P. He, Y. Xu, X. Kou, Z. Yu, X. Xie, P. Miao, *Sens. Actuators, B* **2020**, *313*, 128015.

[37] K. M. Koo, L. G. Carrascosa, M. J. A. Shiddiky, M. Trau, *Anal. Chem.* **2016**, *88*, 6781.